International Journal of Thermal Sciences 48 (2009) 1683–1695

Contents lists available at ScienceDirect

International Journal of Thermal Sciences

journal homepage: www.elsevier.com/locate/ijts

Natural convection in a square enclosure with a hot source

M. Paroncini*, F. Corvaro*

Dipartimento di Energetica, Università Politecnica delle Marche, Via Brecce Bianche, 60100 Ancona, Italy

ARTICLE INFO

Article history:
Received 15 July 2008
Received in revised form
3 February 2009
Accepted 5 February 2009
Available online 18 March 2009

Keywords:
Natural convection
PIV
Holographic interferometry
Numerical simulation

ABSTRACT

The aim of this paper is to analyse the convective heat transfer generated by a source with three different heights (ζ). This strip is located in the middle of a square enclosure. In detail the experimental analysis was carried out using holographic interferometry, to study the effect of the heat transfer, and a 2D-PIV system, to analyse the dynamic behaviour of the phenomenon. The comparison is based both on the evaluation of the Nusselt numbers at different Rayleigh numbers and on the study of the velocity fields at the same Rayleigh numbers in different configurations. During the experimental analysis we can see how the height of the strip influences the distribution of the velocity fields and consequently the heat transfer efficiency. Three different heights are analysed: $\zeta = 0$, $\zeta = 0.25$ and $\zeta = 0.5$. The study shows how the natural convective heat transfer worsens with the increase in the source height. This can clearly be seen by analysing the upper side of the strip, which was studied for each geometrical configuration, and is also confirmed by the results on the lateral sides, analysed only for $\zeta = 0.25$ and $\zeta = 0.5$.
Finally the experimental data are compared with the results obtained through a numerical simulation performed using the volume finite software, Fluent 6.3.26. The aim of this comparison is to validate the numerical procedure, which is useful for enlarging the Rayleigh number range.

1. Introduction

Natural convection in a square cavity plays a very interesting role in numerous engineering applications, such as solar energy systems, cooling of electronic circuits, air conditioning and many others and is therefore very important for applied research. Technical literature presents a great number of studies on natural convection in a square cavity and many of them analyse the convective phenomenon through numerical simulation. For example, Bourich et al. [1] made a numerical study on the two-dimensional double diffusive natural convection in a square porous cavity partially heated from below while its upper surface was cooled at a constant temperature. Ramos and Milanez's [2] paper deals with the natural convection in cavities heated from below by a thermal source, which dissipated energy at a constant rate. Nibarufata et al. [3] analysed numerically the natural convection in partitioned enclosures with localized heating from below while Valencia and Frederick [4] elaborated a numerical investigation on the heat transfer of air in square cavities with partially active vertical walls and Aydin and Yang [5] simulated numerically the natural convective heat transfer in air in a square cavity cooled from the sidewalls and heated by a strip placed at the middle of the bottom wall. A numerical and experimental study was conducted by Chu and Hichox [6] to simulate the natural convection of high-density fluid variations in cavities with concentrated heating. Cesini et al. [7] analysed the convective heat transfer generated by a horizontal cylinder located in a square cavity. This study was carried out through both experimental analysis and a numerical study.

However, simultaneous applications of Particle Image Velocimetry (PIV) and holographic interferometry have received relatively little attention due to technical difficulties, as already underlined by Lee and Kim [8].

The aim of this paper is to analyse the natural convective heat transfer in a cavity heated by a strip using both types of experimental equipment (holographic interferometry and 2D-PIV) and a numerical code. The cavity tested in this study is a square enclosure; in particular the influence of the height of a heated strip on the natural convection heat transfer is analysed. The experimental results were compared with the results of the numerical analysis obtained through a finite volume code: Fluent 6.3.26. This comparison was performed to validate the numerical model.

* Corresponding authors. Tel.: +39 0712204276/4762 fax: +39 071 2204770.
E-mail addresses: m.paroncini@univpm.it (M. Paroncini), f.corvaro@univpm.it (F. Corvaro).

1290-0729/$ – see front matter © 2009 Elsevier Masson SAS. All rights reserved.
doi:10.1016/j.ijthermalsci.2009.02.005

Nomenclature

d	position of the heat source [m]
g	modulus of the gravity vector [m s^{-1}]
H	square cavity side [m]
k	thermal conductivity [W m^{-1} K^{-1}]
l	heat source length [m]
L	cavity depth in the experimental tests [m]
T	temperature [K]
x	Cartesian axis direction [m]
y	Cartesian axis direction [m]
Pr	Prandtl number
Ra	Rayleigh number
Nu_h	local Nusselt number
Nu_{ave}	average Nusselt number
X	dimensionless Cartesian axis direction
Y	dimensionless Cartesian axis direction

Greek symbol

β	thermal expansion coefficient [K^{-1}]
δ	dimensionless position of the heat source
ε	dimensionless length of the heat source
θ	dimensionless temperature
ζ	dimensionless height of the heat source
υ	kinematic viscosity [m^2 s^{-1}]
ρ	density [kg m^{-3}]

Subscripts

c	cold wall
h	hot wall
exp	experimental data
num	numerical data
rg	right side of the source
lf	left side of the source

2. Experimental equipment

2.1. Holographic interferometry

The main components of the experimental apparatus, shown in Fig. 1, include the test cell, filled with air at atmospheric pressure, the pneumatic auto levelling table, the holographic interferometer, the optical instruments, three thermostatic baths and the data acquisition system.

The enclosure has a square transversal section with sides of 0.05 m in length. It is heated from below with a heat source made of aluminium with a thickness of 0.01 m and maintained at a temperature T_h by a fluid that circulates through one of the three thermostatic baths. This temperature was changed from one test to another to obtain different Rayleigh numbers. The lateral vertical walls (made of aluminium) are kept at a constant temperature T_c by a fluid, which is cooled by two other thermostatic baths. In this case the temperature was kept constant during each test and was set at 291.16 K. The top and the bottom surfaces of the enclosure are made of plexiglas to prevent heat leakage through these walls. However, since this is not feasible in the experimental analysis the boundary condition at these surfaces was implemented in order to take into account the conductive heat flux through the plexiglas walls. The end vertical walls are made of glass to guarantee access of the laser beam. A scheme of the enclosure is shown in Fig. 2.

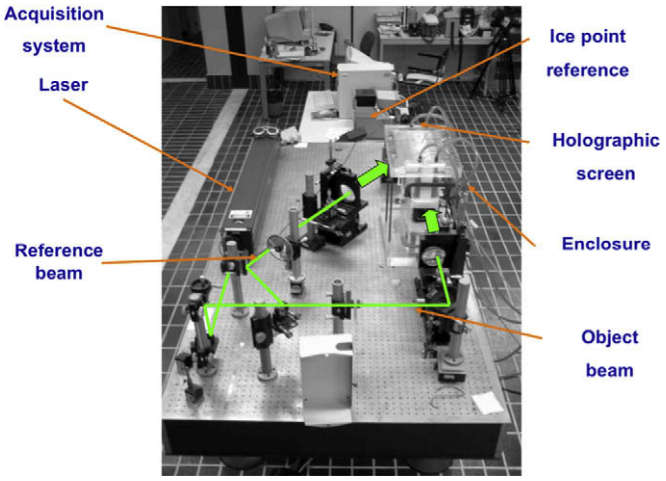

Fig. 1. Holographic interferometry system.

The dimension of the test cell along the longitudinal direction is 0.42 m, which allows the end effects to be neglected and the problem to be considered from a two-dimensional point of view.

The thermostatic circuit is made up of two thermostats with their respective connecting pipes. The PROLINE RP1840 thermostats are manufactured by Lauda Company; the main characteristics of this model are shown in Table 1. Each pipe, which connects the thermostats with the inlet and outlet valves of the two sidewalls and the heater, is covered with a neoprene skin (about 0.02 m thick) to insulate it from heat loss. The thermostatic fluid is a mixture of 75% water and 25% glycol. The same system is used in the PIV analysis.

The acquisition system is made up of fourteen copper–constantan thermocouples that are inserted to measure the temperature on the vertical walls and on the heated strip. Three thermocouples are placed on the source and ten are set on the vertical walls. Each thermocouple is connected with an ice point

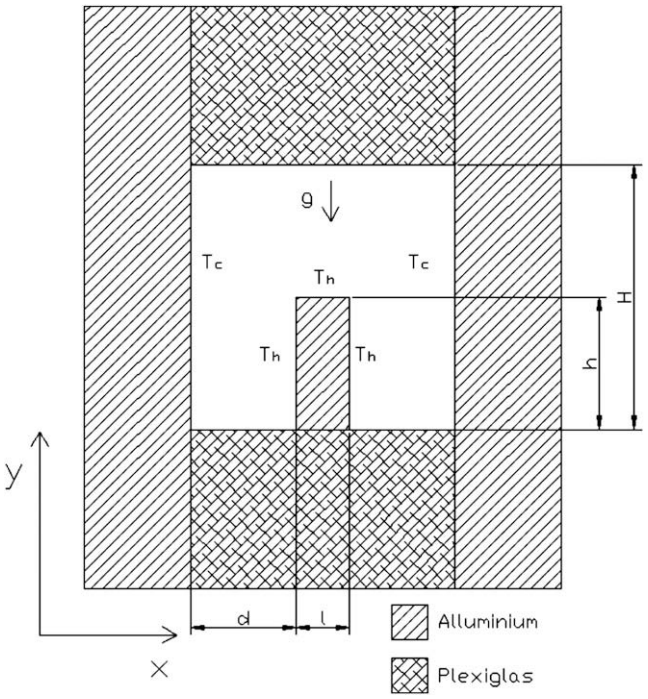

Fig. 2. Test cell.

Table 1
Main characteristics of thermostat.

Operating temperature range (°C)	−40 to 200
Temperature accuracy (±°C)	0.01
Bath volume (*l*)	18
Class to EMC standard	B according to EN61326-1

reference made by Kaye, model K170. All the thermocouples are located 1 mm under the surface of the test volume and they check the surface temperatures. Unfortunately these temperatures cannot be used directly to obtain the temperature distribution of the fringes during the interpretation of the interferograms since, because of diffraction effects, the position of both the heater and the sidewalls is uncertain. For this reason the last thermocouple is positioned in the middle of the air region in order to give us a reference temperature for analysing the interferograms. In the following PIV analysis this last thermocouple was removed to permit the access of the laser light in the middle of the cavity. The difference between the three temperature values on the aluminium plate is about 0.2 K and therefore it is possible to consider an isotherm situation; on the lateral wall the maximum difference between the five thermocouples is 0.4 K. All the temperature values show a maximum uncertainty, due to the measurement system, of ±0.1 K.

The results of the temperature measurements are stored by a data acquisition system. This system is made up of a computer, to store the measurements, and a data acquisition/switch unit, model Hp Agilent 34970A, to read-in the temperature values. The same measurement apparatus is used in the PIV set-up.

The light source is an argon-ion laser with a nominal power rating of 4 W, with etalon for the 514.5 nm wavelength. Both object and reference beams have a maximum diameter of 0.15 m. The optical set-up allows us to use either double-exposure or real-time holographic interferometry techniques for the steady-state and temporal evolution measurements of heat transfer processes. The real-time technique was also used to check the presence of plume oscillations.

The real-time interferograms are obtained through a fringe finite field, while a fringe infinite field is used in the double-exposure interferograms; in this way the fringe pattern is comparable to the distribution of the isothermal lines. The density and temperature distributions are obtained using the inversion method [9]. The evaluation of the interferograms is achieved through the help of an optical microscope; according to Hauf and Grigull [9], the expected accuracy for small fringe numbers (less than 30) can be about 10%.

2.2. PIV set-up

The test cell, the acquisition system and the thermostatic elements are the same as those used in the holographic set-up. The whole system is shown in Fig. 3.

Particle Image Velocimetry (PIV) is finalized to make instantaneous velocity measurements in the cross-section of a flow. The PIV system provides the velocity fields with the distance covered by the particles seeded in the flow. The nature of the seeding particles must be chosen in order to provide a real description of the air flow. The measurement principle of particle image velocimetry has been presented in numerous papers and technical books in scientific literature such as Raffel et al. [10].

In this experiment the oil particles have a diameter of about 1 μm and are nebulized by the air pressure system. The laser used is a double cavity Nd–Yag laser with a wavelength of 532 nm.

Data analysis was performed using the software package "Dynamic Studio", provided by Dantec Dynamics [11].

The images of the area of the flow field, lit up by a light sheet, are captured by a CCD camera (Hammatsu camera C8484-05C with 1344×1024 number of pixels). The camera lens was covered by a filter with a wavelength $\lambda = 532$ nm in order to record only the direct or scattered light from the laser source inside the PIV cavity.

The light sheet enters through the upper part of the enclosure made of plexiglas and lights up a cross-section of the cavity in the middle of the cell. The camera, that is located perpendicular to the light sheet, captures the images, which are sent to a computer to be processed.

The front sidewall of the cavity is covered by a small pane of glass to permit optical access to the camera while the rear side is rigged with a 0.05 m square piece of wood which has an opening in the middle. The oil particles are sprinkled through this opening 20 s before the beginning of each test. The top and the bottom surfaces of the enclosure are made of plexiglas with a thickness of 0.03 m to prevent the heat from leaking through these surfaces. The Rayleigh numbers analysed range from 6.5×10^4 to 3.2×10^5.

The processing technique used in this study is Dantec's adaptive cross-correlation, described by Dantec Dynamics [11], with an interrogation area of 32×32 pixels.

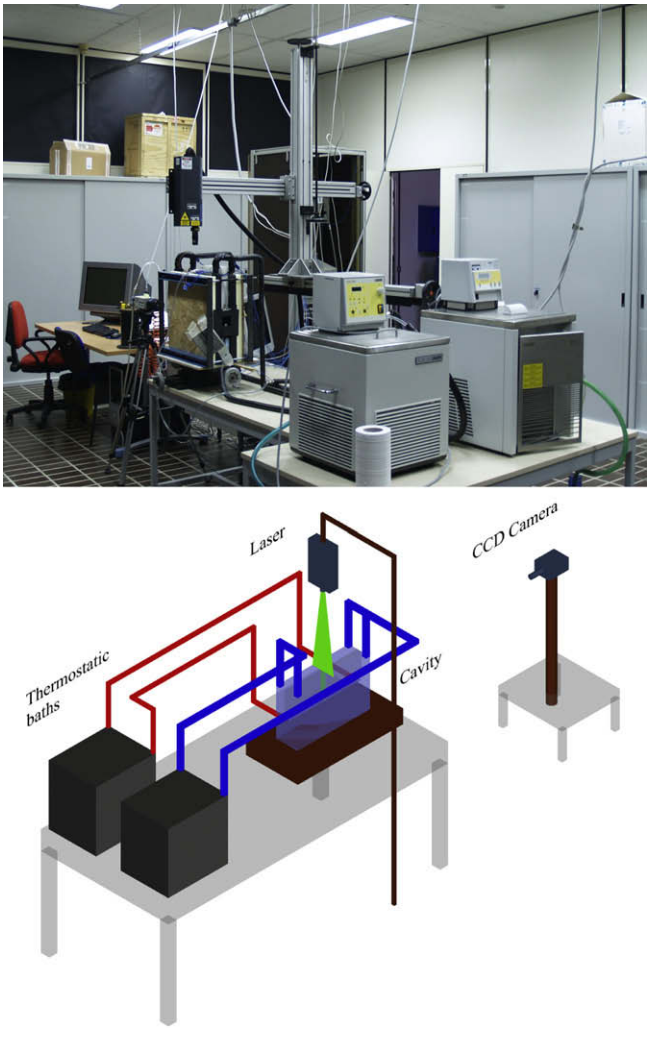

Fig. 3. 2D-PIV system.

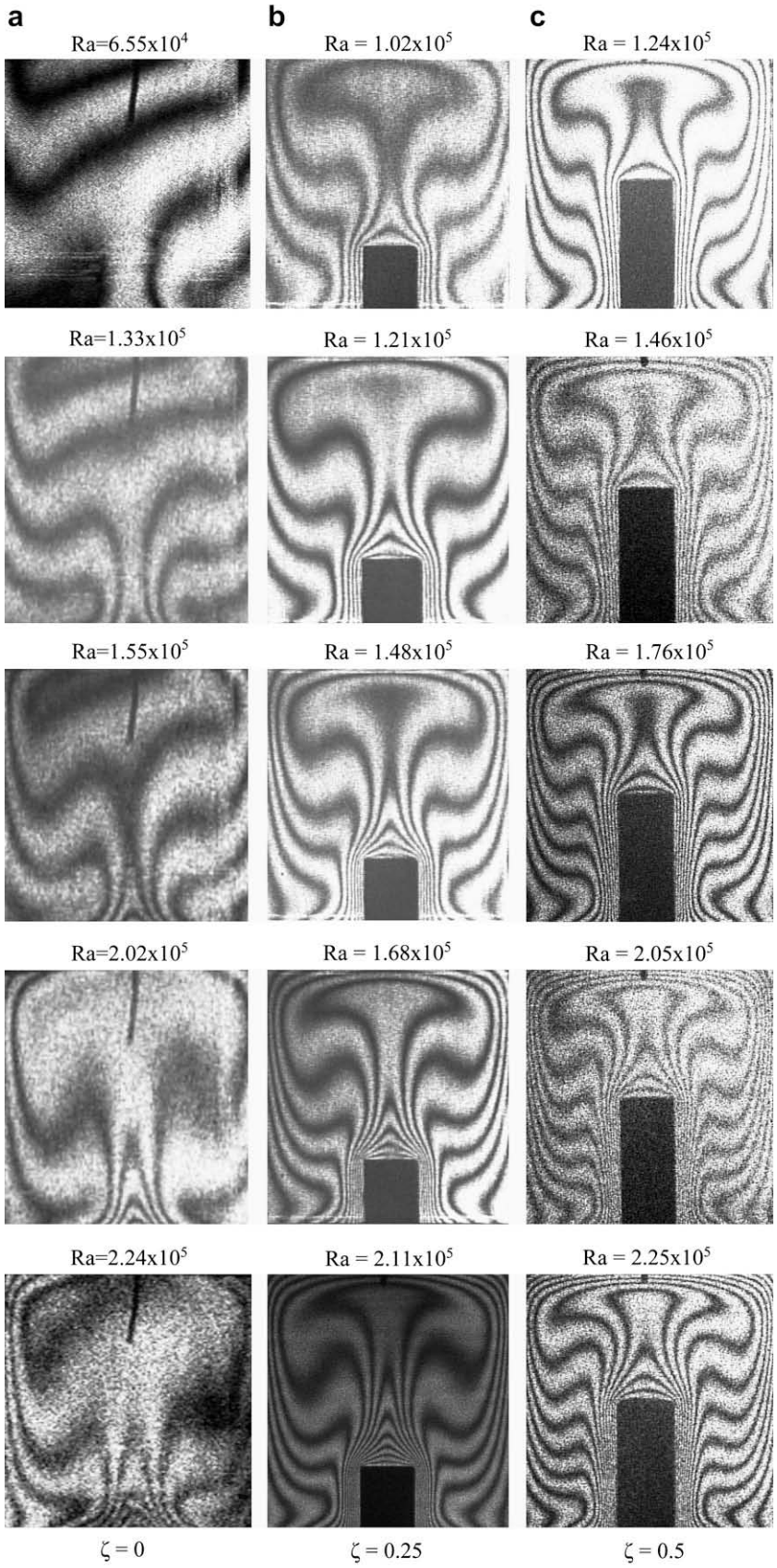

Fig. 4. Experimental double-exposure interferograms.

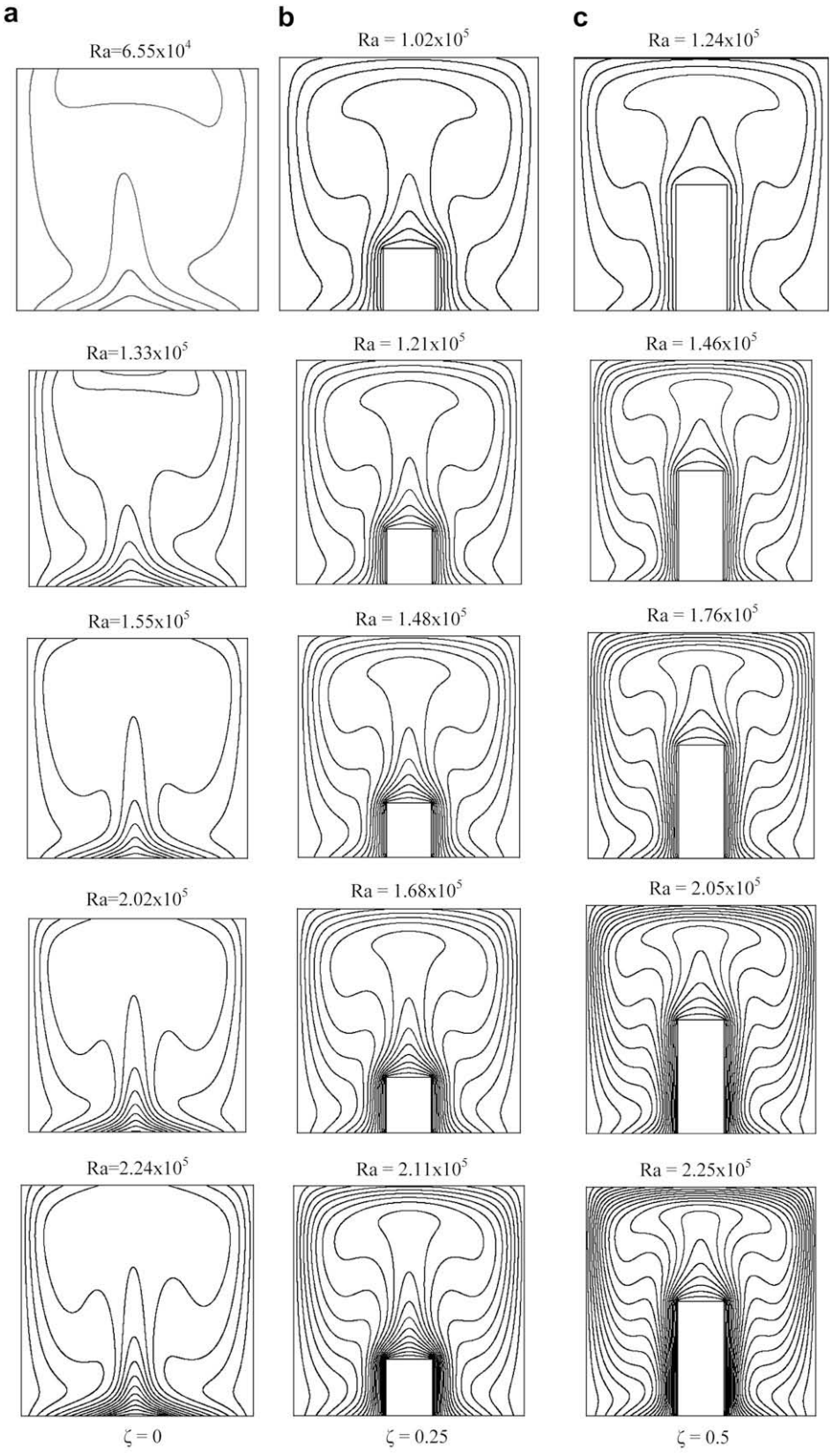

Fig. 5. Numerical isothermal lines.

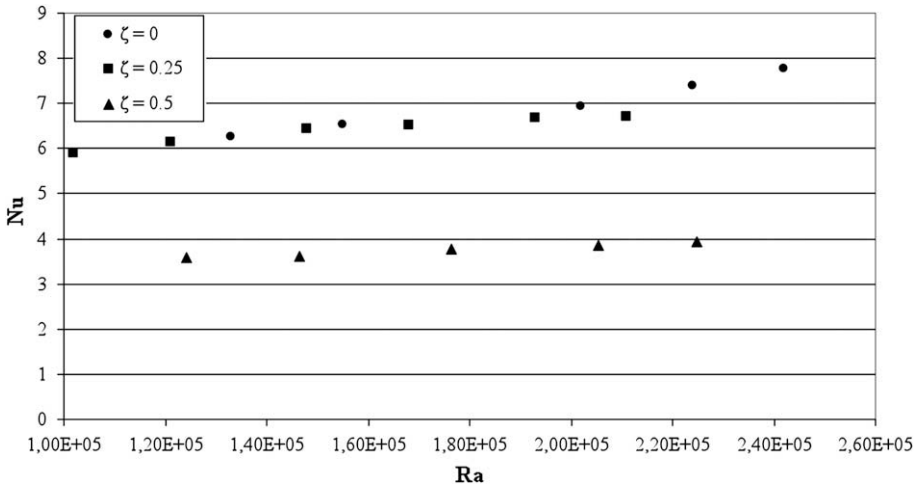

Fig. 6. Experimental average Nusselt number as a function of the Rayleigh number on the upper surfaces.

The overlap of the interrogation area in the horizontal and in the vertical direction is 50%. Furthermore, a moving average validation is applied; this method validated the vectors based on the comparison between neighbouring vectors; an averaging area of 3×3 is used with an acceptance factor of 0.1 and there are 3 iterations. This method substituted outliers due to false correlations resulting from reflections at the cell walls and the other invalid vectors.

The laboratory where the tests were carried out is air-conditioned so it is possible to check and to decide the room temperature and the humidity conditions: for each test the room temperature was set at 297 K with 50% relative humidity.

Before the beginning of each experiment the seal of the cavity was checked to avoid any seeding leakage.

After these preliminary controls the thermostatic baths, set at the correct temperatures, were turned on. At this stage the thermostatic circuits were closed. When the thermostatic fluids inside each bath reached the target temperature the valves were opened to permit circulation in the cold walls and in the internal source. The acquisition system was then also started so as to record the temperature trend on the lateral walls and on the hot strip. Using this system it is possible to check when the cold surfaces and the hot one reach the isothermal condition. At this point the flow stability inside the cavity starts to be checked. Twenty seconds before the beginning of image acquisition, the oil particles are sprinkled inside the cavity through the small hole on the back side of the upper plexiglas surface.

At this stage it is very important to check carefully that, after the introduction of the seeding, which generates a perturbation in the air motion inside the cavity, the perturbation disappears and the flow reaches the steady state again. This happens in a very short time (10–15 s after the sprinkling), showing a very high physical stability of the studied phenomenon in these specific configurations.

The other important step, that needs to be followed carefully, is the choice of time between two different laser pulses.

In the experiments performed using the PIV technique, this time is one of the most important parameters to set since if this parameter is not correct the time between two different frames is either too short or too long to record the correct displacement of each particle, and consequently it is impossible to evaluate the velocity field of the flow analysed.

3. Numerical procedure and setting

Fluent solution methods are well known in the scientific field. In this study the numerical simulation is developed with the finite

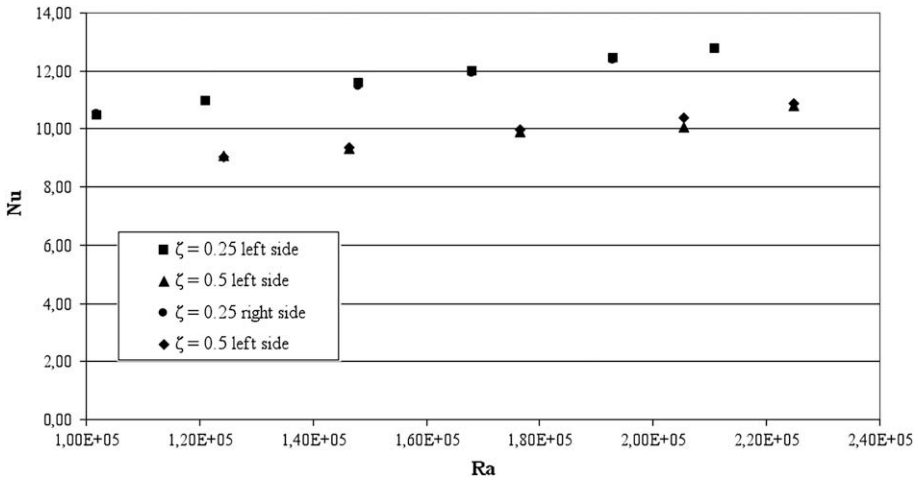

Fig. 7. Experimental average Nusselt number as a function of the Rayleigh number on the lateral surfaces.

Table 2
Comparison between experimental and numerical average Nusselt numbers at different Rayleigh numbers for $\zeta = 0$.

$\zeta = 0$			
Ra_{exp}	Nu_{exp}	Nu_{num}	Δ%
1.33×10^5	6.26	6.23	0.43%
1.55×10^5	6.51	6.55	−0.67%
2.02×10^5	6.93	7.15	−3.14%
2.24×10^5	7.37	7.39	−0.33%
2.42×10^5	7.75	7.58	2.14%

volume code Fluent 6.3.26 using the Boussinesq approximation for the air and a two-dimensional model.

The numerical results are found through the segregated solvers [12] for $3 \times 10^4 < Ra < 3.5 \times 10^5$. According to this approach the governing equations of continuity, momentum and energy are solved sequentially, segregated from one another. Following this method, each discrete equation is linearized implicitly with respect to the equation's dependent variable.

As regards the spatial discretization, in our tests a second order implicit upwind scheme is adopted for the conservation equations; the pressure interpolation is provided by the Body Force Weighted scheme and the pressure–velocity coupling is obtained using the SIMPLE algorithm. The diffusion terms are central-differenced with a second order accuracy and a two-dimensional model is used with the condition of laminar flow.

In the analysis performed the cavity was reproduced with the real dimensions, and the temperature of the lateral walls and of the heated strip was assigned. The plexiglas elements used to make the upper and the lower surfaces of the experimental enclosure were also introduced in the Fluent model. It was necessary to simulate the conductive heat transfer between these elements and the cold wall.

A mesh structure with quadrilateral cell elements was developed. A study of the mesh was carried out preliminarily to obtain the lowest number of cells necessary to perform an analysis with results, which are independent from the choice of the cell number.

During this step it is possible to note that a good mesh is necessary to solve important dynamic structures. In particular with the PIV system very small vortexes are evident on the upper surface of the hot strip with $\zeta = 0.5$. To evaluate them a mesh of 1,000,000 cells in the enclosure area is used. Under these conditions the variables used to compare the numerical results and the experimental ones (such as the local and average Nusselt numbers or the heat flux) showed an independent behaviour with respect to the grid size and any particular dynamic structure can be solved.

The simulations started with the fluid at a uniform and constant temperature (T_{start}) that is a linear weighted average of the heat source and the temperatures of the cold walls; in this way it is possible to avoid the formation of an anomalous convective flux before reaching the steady condition.

Steady and unsteady solvers are both used in the investigation. During the steady procedure the admitted value to obtain convergence was 10^{-6} for the equations of continuity and momentum while it was lower than 10^{-12} for the energy equation. In the unsteady technique the admitted value for convergence was 10^{-11}.

The unsteady procedure allows the analysis of possible motion periodicities or instabilities. The dimensionless time step used varies from 10^{-4} to 10^{-6}, and the number of time steps was chosen sufficiently high to have an asymptotic steady-state solution. In the unsteady solvers the maximum number of iterations per time step is generally high enough to reach the grid limit of calculation with a constant value for all the residuals.

The local and average Nusselt numbers on the hot surfaces, the velocity fields, the stream functions and the velocity vector distribution inside the cavity obtained numerically were compared with the experimental results.

4. Results and discussion

4.1. The interferometric analysis

The study deals with the effects of the height of a hot source on the natural convective heat transfer; the length of the source is 1/5 of the side of the enclosure and it has the same longitudinal length as the enclosure. Three different heights are analysed: $\zeta = 0$, $\zeta = 0.25$ and $\zeta = 0.5$.

The Rayleigh numbers investigated vary from about 1.24×10^5 to 2.25×10^5.

The dimensionless parameters used are:

$$X = \frac{x}{H};\ Y = \frac{y}{H};\ \theta = \frac{T - T_c}{T_h - T_c};\ \varepsilon = \frac{l}{H};\ \zeta = \frac{h}{H};\ \delta = \frac{\left(d + \frac{l}{2}\right)}{H}. \quad (1)$$

For each Rayleigh number analysed the hot strip is located on the bottom of the enclosure with a distance from the sidewalls of $\delta = 0.5$ of the side of the enclosure (symmetrical position).

The local Nusselt number – Nu(X) – is calculated on the heat source with the expression:

$$Nu_h(X) = -\left.\frac{\partial\theta}{\partial Y}\right|_{Y=0} \quad (2)$$

for the upper surface of the strip, while for the lateral side of the source at different heights the following expression is used:

$$Nu_h(Y) = -\left.\frac{\partial\theta}{\partial X}\right|_{X=0} \quad (3)$$

Table 3
Comparison between experimental and numerical average Nusselt numbers at different Rayleigh numbers for $\zeta = 0.25$.

$\zeta = 0.25$									
Ra_{exp}	Nu_{exp}, rg	Nu_{num}, rg	Δ%	Nu_{exp}, lf	Nu_{num}, lf	Δ%	Nu_{exp}, up	Nu_{num}, up	Δ%
1.02×10^5	10.49	10.46	0.25%	10.46	10.46	−0.04%	5.9	6.16	−4.33%
1.21×10^5	10.96	10.96	−0.02%	10.99	10.96	0.24%	6.14	6.27	−2.19%
1.48×10^5	11.46	11.58	−1.06%	11.43	11.58	−1.35%	6.45	6.42	0.50%
1.68×10^5	11.89	11.99	−0.82%	11.91	11.99	−0.69%	6.51	6.51	0.00%
1.93×10^5	12.34	12.45	−0.89%	12.32	12.46	−1.10%	6.67	6.61	0.87%
2.11×10^5	12.71	12.76	−0.36%	12.74	12.76	−0.17%	6.72	6.68	0.62%

Table 4
Comparison between experimental and numerical average Nusselt numbers at different Rayleigh numbers for $\zeta = 0.5$.

$\zeta = 0.5$									
Ra_{exp}	Nu_{exp}, rg	Nu_{num}, rg	Δ%	Nu_{exp}, lf	Nu_{num}, lf	Δ%	Nu_{exp}, up	Nu_{num}, up	Δ%
1.24×10^5	9.04	8.98	0.61%	9.07	8.98	1.00%	3.58	3.67	−2.57%
1.46×10^5	9.38	9.40	−0.19%	9.32	9.39	−0.78%	3.62	3.74	−3.38%
1.76×10^5	9.98	9.89	0.90%	9.9	9.89	0.14%	3.78	3.82	−1.15%
2.05×10^5	10.4	10.31	0.87%	10.06	10.31	−2.45%	3.85	3.89	−1.07%
2.25×10^5	10.86	10.57	2.68%	10.8	10.57	2.16%	3.93	3.93	−0.05%

The average Nusselt number – Nu_{ave} – on the heat source is given for the upper surface of the source by:

$$Nu_{ave} = \frac{1}{\varepsilon}\int_0^{\varepsilon} Nu_h(X)dX. \quad (4)$$

while for the lateral surfaces the expression used is:

$$Nu_{ave} = \frac{1}{\zeta}\int_0^{\zeta} Nu_h(Y)dY. \quad (5)$$

In the first part of the study holographic interferometry was used to analyse the heat transfer inside the enclosure. Using the real-time exposure technique reaching steady state could be studied. The double-exposure technique was then used to obtain the double-exposure interferograms.

Analysing the images in Fig. 4 some examples of double-exposure interferograms can be seen. The different black and white lines are comparable to isothermal lines: each line is characterized by a different temperature level. This level changes starting from the hot source which is put in the middle of the enclosure. The asymmetrical behaviour of some interferograms is probably connected both with the conductive heat transfer of the plexiglas upper surface and with some experimental inaccuracies. But this effect is confined to the upper part of the cavity so it does not have a big influence on the hot strip where the Nusselt numbers are evaluated.

Through the central thermocouple, as described in Section 2, it is possible to associate a temperature value with a specific fringe. The whole temperature fields in the cavity can then be calculated.

Fig. 5 shows the same images obtained through the numerical code. In both cases it is possible to see that there are a lot of fringes near the lateral sides of the hot source for $\zeta = 0.25$ and for $\zeta = 0.5$. From a qualitative point of view, compared with the upper surfaces, these elements show a strong heat transfer. Finally it is possible to find a good agreement between the numerical results and the experimental ones even if several interferograms show some asymmetrical distribution of the fringes due to experimental inaccuracy. This is more evident for the lowest Rayleigh numbers.

A quantitative analysis was also carried out: the local Nusselt numbers on each hot surface were evaluated. The average Nusselt numbers for different Rayleigh numbers were calculated using these data. An example of this procedure is shown in Fig. 6 where it is possible to find the experimental average Nusselt number as a function of the Rayleigh number on the three upper surfaces studied. Analysing this graph, a great difference between the three heights can be noted. At $\zeta = 0$ and $\zeta = 0.25$ the trend in the average Nusselt number is almost constant: the same values are found for each Rayleigh number analysed; only for the highest Rayleigh numbers does the average Nusselt number for $\zeta = 0$ seem to grow more quickly than for $\zeta = 0.25$. However, for $\zeta = 0.5$ lower average Nusselt numbers were recorded on the upper side of the source. These values are very close to half of the previous values. This result is very important because it indicates that for $\zeta = 0.5$ the upper surface has a worse heat transfer than the other two geometrical configurations analysed. It is interesting to understand why there is a strong reduction in heat transfer efficiency. Using the interferometric analysis it is difficult to explain this fact even if it is very useful for quantifying the reduction value in the Nusselt number. Therefore an in-depth study using the PIV system should be made in order to point out any possible dynamic structure, which could influence the heat transfer on this surface (at $\zeta = 0.5$).

Fig. 7 shows the average Nusselt number as a function of the Rayleigh number on the lateral sides both for $\zeta = 0.25$ and for $\zeta = 0.5$. It is possible to note the symmetric behaviour of the two surfaces for each height analysed. It is also important to underline a difference between the values recorded for $\zeta = 0.25$ and for $\zeta = 0.5$. Larger average Nusselt numbers were recorded for the sides with the lowest height ($\zeta = 0.25$) compared with the numbers found for the other heights. Therefore there is a more efficient heat

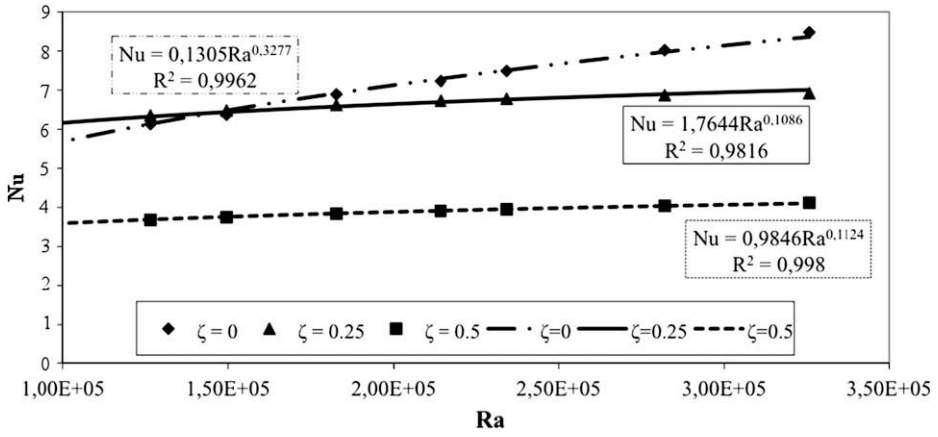

Fig. 8. Numerical correlation between the Rayleigh numbers and the average Nusselt numbers on the upper surfaces.

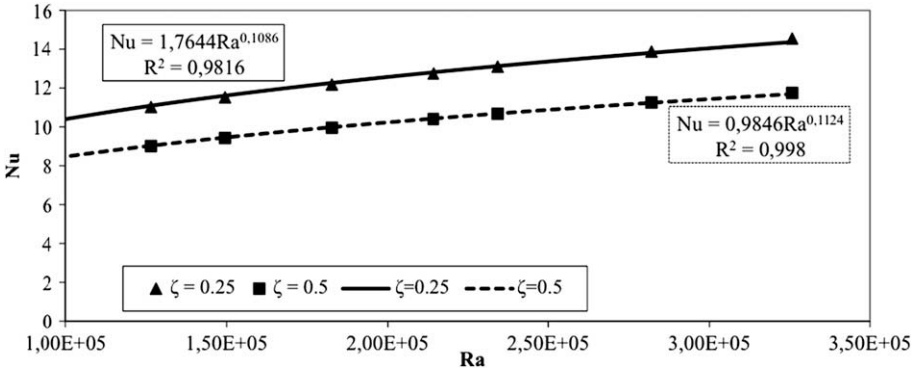

Fig. 9. Numerical correlation between the Rayleigh numbers and the average Nusselt numbers on the left surfaces.

transfer for $\zeta = 0.25$ than for $\zeta = 0.5$. As underlined in the previous case, an in-depth PIV analysis would be very useful to explain this aspect.

It is also important to make a comparison between the numerical data and the experimental ones in order to use the code to extend our analysis. The comparison is shown in three different tables: Table 2 presents the results for $\zeta = 0$, Table 3 those for $\zeta = 0.25$ and Table 4 the others for $\zeta = 0.5$.

By analysing these results it is possible to note how the percentage difference between the experimental value of the average Nusselt number and the numerical value for the same Rayleigh number is lower than 5%. In particular the worst result (4.33%) is recorded for $\zeta = 0.25$ at $\mathrm{Ra} = 1.02 \times 10^5$.

These data show a good agreement between the experimental structure and the numerical set-up so the numerical code can be used to extend our analysis and to obtain an empirical correlation between the average Nusselt number and the corresponding Rayleigh number.

The law used to connect these two dimensionless numbers is

$$\mathrm{Nu_{ave}} = a \cdot \mathrm{Ra}^b, \tag{6}$$

where a and b change according to the hot surface analysed.

These relationships are shown both in the graph in Fig. 8, for the upper surfaces, and in the graphs in Figs. 9 and 10, for the lateral sides. In these graphs it is also possible to see the R^2 for each correlation used. R^2 is an indicator that shows the agreement between the estimated and the real values of the empirical function. The closer R^2 is to 1, the more the relationship can be considered a good real data approximation.

$$R^2 = 1 - \frac{\mathrm{SSE}}{\mathrm{SST}}. \tag{7}$$

where SSE is

$$\mathrm{SSE} = \sum_{j=1}^{n} \left(K_j - \widehat{K}_j\right), \tag{8}$$

where K_j is the real point on the graph, n is the number of the points analysed and $\widehat{K}_j$ is the corresponding point on the model of the empirical function. It is therefore possible to define SST as

$$\mathrm{SST} = \left(\sum_{j=1}^{n} K_j^2\right) + \frac{1}{n}\left(\sum_{j=1}^{n} K_j\right)^2. \tag{9}$$

The graphs confirm the observations made using the experimental results. In particular it is important to underline the stronger growth in the average Nusselt numbers at the highest Rayleigh numbers with respect to those recorded on the same side at $\zeta = 0.25$, as is also confirmed for the upper surface at $\zeta = 0$.

4.2. The PIV analysis

Thermal behaviour was studied using the 2D-PIV system to analyse the natural convective heat transfer from a dynamic point of view. In particular it is possible to explain the reason for some thermal aspects shown in Section 4.1.

Some different tests were made at different Rayleigh numbers and the results are shown in the figures. For example, in Fig. 11 it is

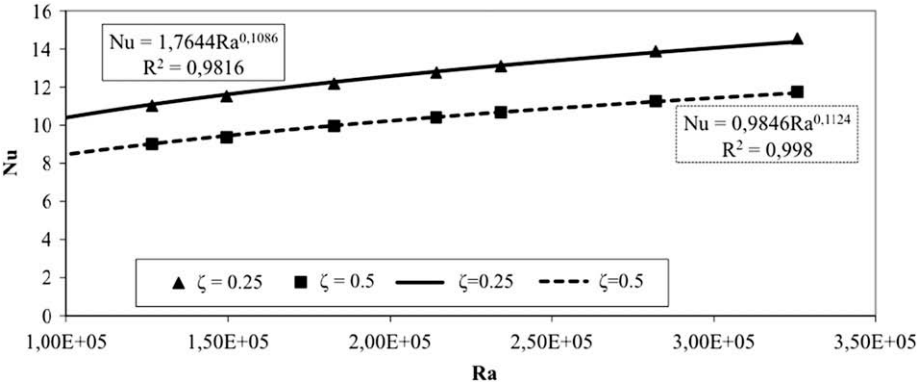

Fig. 10. Numerical correlation between the Rayleigh numbers and the average Nusselt numbers on the right surfaces.

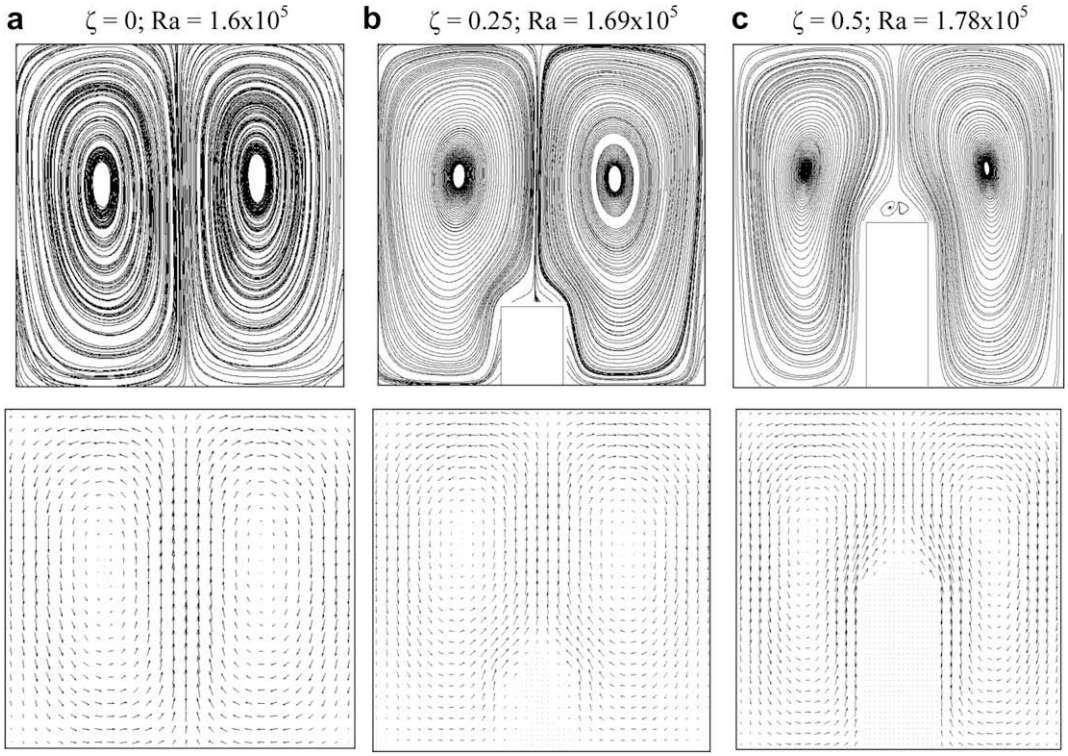

Fig. 11. Experimental streamlines (first row) and experimental velocity vector distribution (second row).

possible to see the streamlines and the velocity vector distributions obtained by the PIV system at different Rayleigh numbers for the three heights analysed. Through our analysis it can be seen that these dynamic structures are not influenced by the change in the Rayleigh numbers. The streamlines and the vector distribution remain constant for each geometrical configuration analysed and the numerical simulation, as shown in Fig. 12, confirmed this result.

Moreover in these images the presence of two big vortexes is evident; they do not rotate in the same direction. They do not change with the Rayleigh number but their shape is influenced by the height of the hot source, as shown in both Figs. 11 and 12. In each case they have a symmetrical behaviour and their rotation axis is parallel to the direction of the depth of the cavity (z axis). Their contact line is perpendicular to the hot strip and agrees with the axis of symmetry of the source both for each Rayleigh number analysed and for each height.

It is very interesting to observe the streamlines in Fig. 11c. Through this image it is possible to explain the reduction in the average Nusselt numbers on the upper surface for $\zeta = 0.5$. This reduction was recorded during the interferometric tests and can

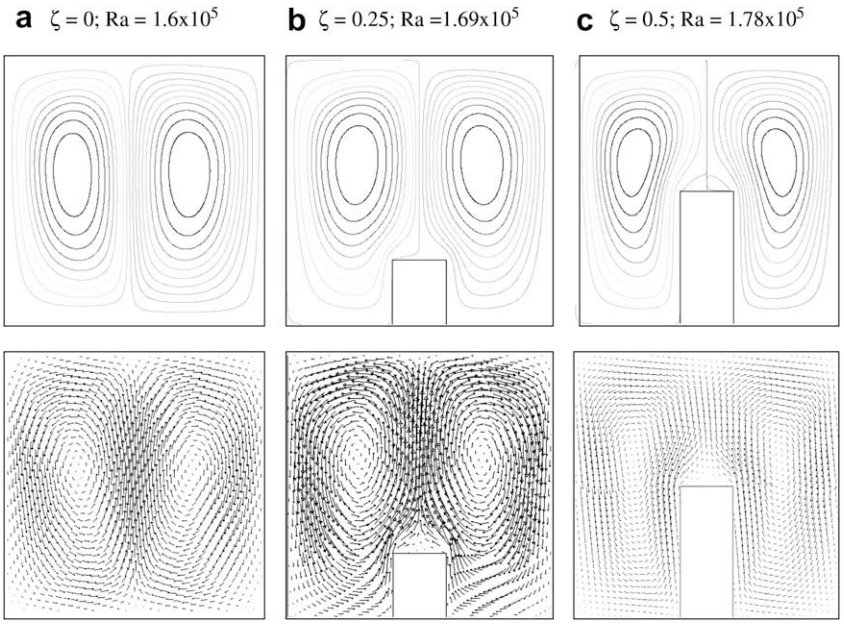

Fig. 12. Numerical streamlines (first row) and numerical velocity vector distribution (second row).

clearly be seen in the graph in Fig. 6. If the streamlines of Fig. 11c are analysed, it is possible to note the presence of two small vortexes on the upper side of the source, which are absent in the other geometrical configurations. These two small vortexes strongly influence the air motion on this side since they create a small recirculating bubble in which the air slackens and consequently the convective heat transfer is reduced. This is confirmed by the velocity map shown in Fig. 13 for $\zeta = 0$, in Fig. 14 for $\zeta = 0.25$ and in Fig. 15 for $\zeta = 0.5$. If the velocity value in this zone for $\zeta = 0.5$ is analysed it is evident that it is lower than the value in the same area for the other geometrical configurations. Therefore, for $\zeta = 0.5$ there are two small vortexes on the upper surface of the source which slacken the air motion and consequently reduce the natural convective heat transfer on this side.

Fig. 12 shows the streamlines and the velocity vector distributions obtained through the numerical simulation. With these images it is possible to see a good agreement between the numerical code and the experimental set-up. This is also evident by analysing the velocity maps for each geometrical configuration, as shown in Figs. 13–15. In these images the first column shows the experimental data obtained using the PIV system while the second column presents the numerical results obtained with the Fluent code.

From these figures it can be seen how the velocity value is strongly connected to both the Rayleigh number and the geometrical configuration. In particular the velocity field increases as the Rayleigh number grows. Analysing these images, it is also possible to explain the different behaviour in the average Nusselt numbers that are recorded on the lateral sides for $\zeta = 0.25$ and for $\zeta = 0.5$. The thermal analysis showed that the average Nusselt numbers on the lateral surfaces for $\zeta = 0.25$ are bigger than those for $\zeta = 0.5$ at the same Rayleigh number. By comparing the velocity maps in Fig. 14 to the ones in Fig. 15 for similar Rayleigh numbers, it is evident that the velocity fields for $\zeta = 0.25$ are quicker than those for $\zeta = 0.5$. This finding, supported by the Fluent code, indicates that in the cavity with a height source of $\zeta = 0.5$ the air motion is slower than is found when the height source is $\zeta = 0.25$. Consequently, in the first geometrical configuration there is worse natural convective heat transfer than in the second configuration. This is in agreement with the difference between the average Nusselt numbers recorded in these two cases.

Moreover, the quickest velocity field, recorded for $\zeta = 0.25$, is connected to the vortexes generated at the different source heights. If both the numerical streamlines (Fig. 12b) and the experimental ones (Fig. 11b) are compared, it is possible to notice that for $\zeta = 0.25$

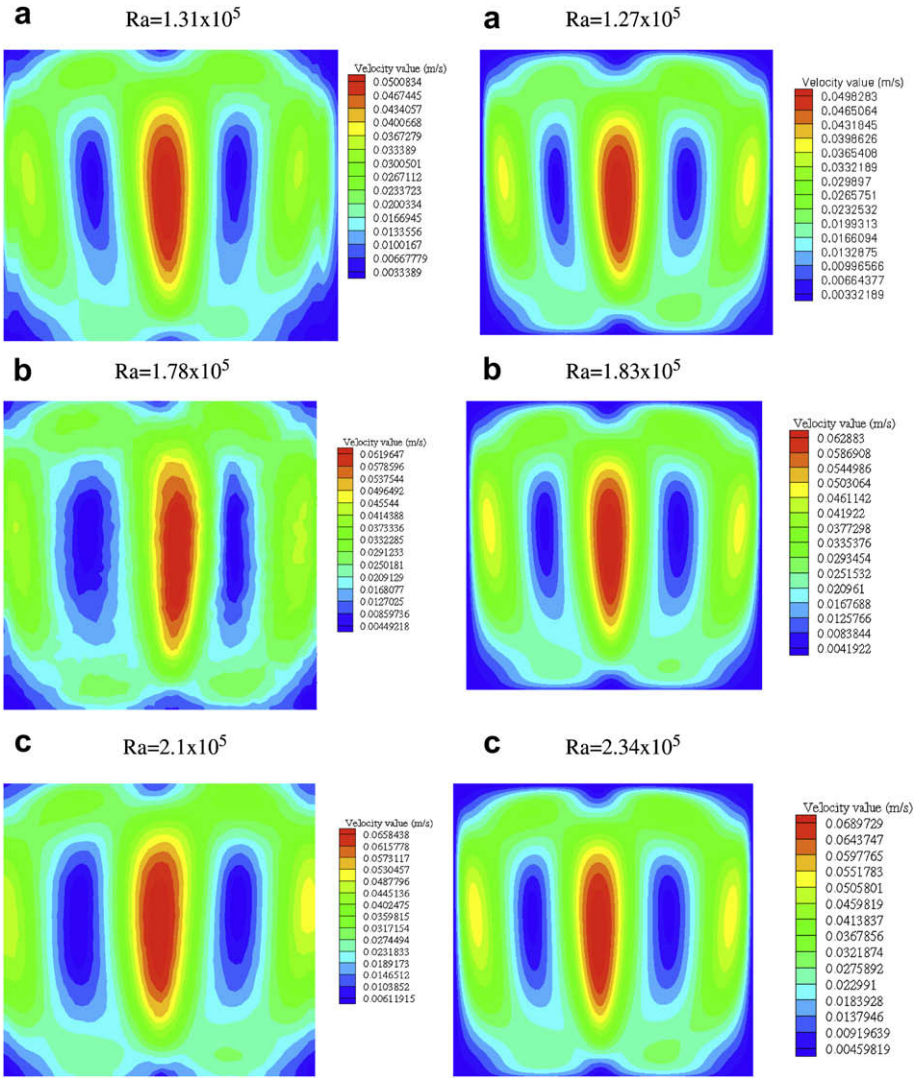

Fig. 13. Experimental velocity maps (first column) and numerical velocity maps (second column) for different Rayleigh numbers for $\zeta = 0$.

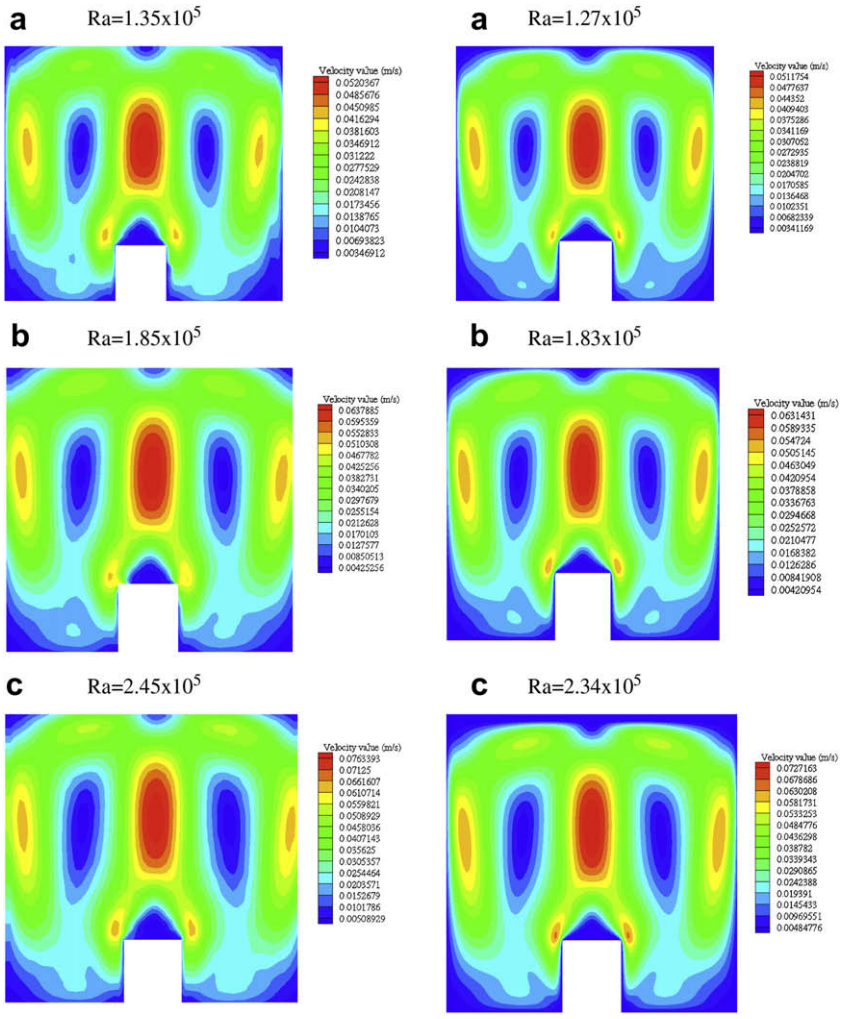

Fig. 14. Experimental velocity maps (first column) and numerical velocity maps (second column) for different Rayleigh numbers for $\zeta = 0.25$.

the two big vortexes come into contact more quickly than for $\zeta = 0.5$ (Figs. 11c and 12c). This reinforces the whole velocity field in the geometrical configuration with $\zeta = 0.25$ and consequently creates a better natural convective heat transfer, as shown by the average Nusselt numbers reported in Fig. 7.

5. Conclusion

This paper analysed the influence of the height of a hot source on the natural convective heat transfer in a square cavity of side $H = 0.05$ m.

The analysis was conducted experimentally, using both holographic interferometry for Rayleigh numbers from 1.2×10^5 to 2.3×10^5 and with Particle Image Velocimetry (PIV) for a Rayleigh number with a variation range from 6.5×10^4 to 3.2×10^5. The PIV analysis gives us flow structures connected with convective phenomena like velocity fields, stream functions and velocity vector distributions while by using holographic interferometry the average and local Nusselt numbers were evaluated. The experimental analysis is connected to the numerical analysis by means of a simulation code with an Ra number range of $3 \times 10^4 < \mathrm{Ra} < 3.5 \times 10^5$.

Three different heights of the source were analysed: $\zeta = 0$, $\zeta = 0.25$ and $\zeta = 0.5$. The hot strip was put on the floor of the enclosure in a symmetrical configuration. In each case analysed the average Nusselt numbers increase with the Rayleigh number. In particular it was demonstrated that on the upper sides analysed there is a big difference between the configuration with height $\zeta = 0.5$ and the two other ones. For $\zeta = 0.5$ the average Nusselt numbers on the upper surface are significantly lower than in the other cases. This is connected with the creation of two small vortexes on this side for $\zeta = 0.5$ as shown with the PIV system.

Another important consideration concerns the heat transfer on the lateral surfaces for $\zeta = 0.25$ and for $\zeta = 0.5$. For these two configurations the behaviour of the average Nusselt numbers is quite different. For $\zeta = 0.25$ the stored Nusselt numbers are bigger than for $\zeta = 0.5$ considering both the experimental and the numerical data. If the PIV system is used to analyse this aspect, it is possible to see how the two big vortexes, which are present in each configuration, come into contact more quickly at a height of $\zeta = 0.25$. Consequently, the whole velocity field tends to become stronger than the one recorded for $\zeta = 0.5$. Therefore it is possible to say that with a height of $\zeta = 0.5$ a worse natural convective heat transfer is present both on the lateral surfaces and on the upper side with respect to a height of $\zeta = 0.5$.

It is also possible to see how at the highest Rayleigh numbers the upper surface of $\zeta = 0.25$ has higher average Nusselt numbers than

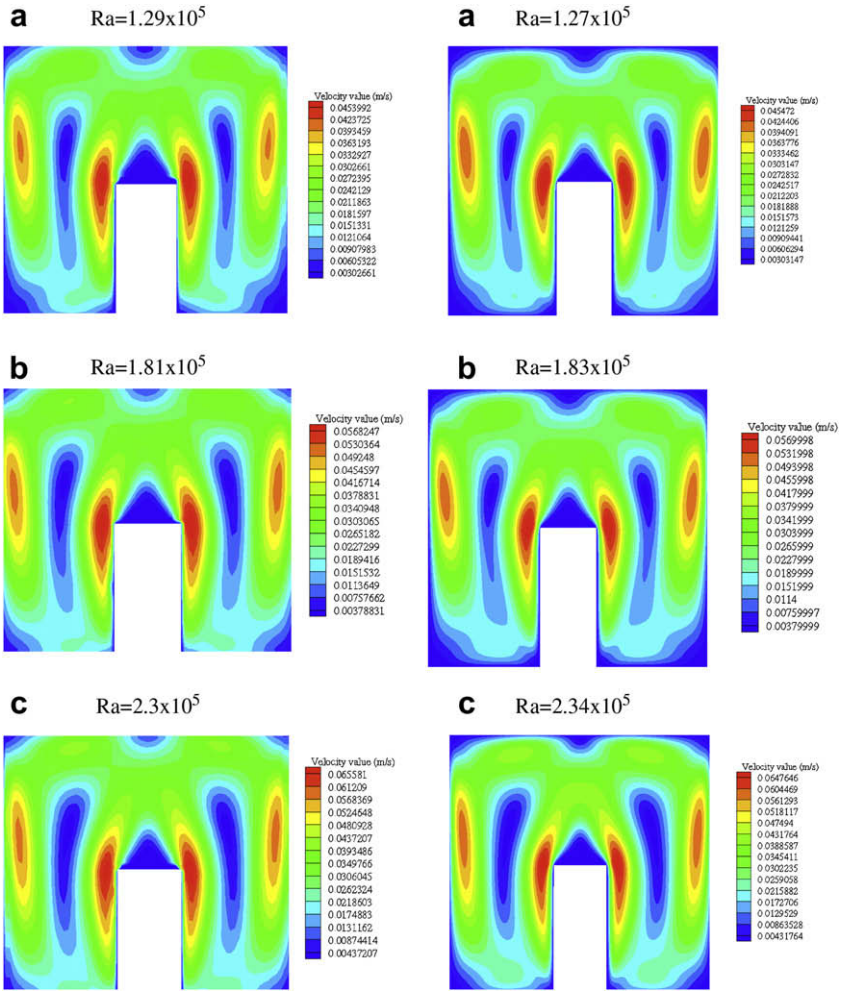

Fig. 15. Experimental velocity maps (first column) and numerical velocity maps (second column) for different Rayleigh numbers for $\zeta = 0.5$.

those found for the same side with $\zeta = 0$. This is evident from both the experimental and the numerical data and indicates a better heat transfer for the geometrical configuration with $\zeta = 0.25$ compared with the other heights analysed.

Moreover with the PIV system it is possible to see how the dynamic structures (streamlines and velocity vector distributions) are not influenced by the change in Rayleigh numbers, while they are strongly connected with the height of the hot strip. Instead the velocity values, shown in the velocity maps, increase with the growth in the Rayleigh numbers in each geometrical configuration analysed.

References

[1] M. Bourich, M. Hasnaoui, A. Amahmid, Double-diffusive natural convection in a porous enclosure partially heated from below and differentially salted, International Journal of Heat and Fluid Flow 25 (6) (2004) 1034–1046.
[2] R.A.V. Ramos, L.F. Milanez, Numerical and experimental analysis of natural convection in cavity heated from below, in: , Proceedings of the 11th IHTC, Kyongju, Korea, vol. 3, 1998.
[3] E. Ntibarufata, M. Hasnaoui, E. Bilgen, P. Vasseur, Natural convection in partitioned enclosures with localized heating, International Journal of Numerical Methods for Heat and Fluid 3 (1993) 133–143.
[4] A. Valencia, R.L. Frederick, Heat transfer in square cavities with partially active vertical walls, International Journal of Heat and Mass Transfer 32 (8) (1989) 1567–1574.
[5] O. Aydin, W.J. Yang, Natural convection in enclosures with localized heating from below and symmetrical cooling from sides, International Journal of Numerical Methods for Heat and Fluid Flow 10 (5) (2000) 519–529.
[6] T.Y. Chu, C.E. Hichox, Heat convection with large viscosity variation in an enclosure with localized heating, International Journal of Heat Transfer 112 (1990) 388–395.
[7] G. Cesini, M. Paroncini, G. Cortella, M. Manzan, Natural convection from a horizontal cylinder in a rectangular cavity, International Journal of Heat and Mass Transfer 42 (1999) 1801–1811.
[8] S. Lee, S. Kim, Application of holographic interferometry and 2D PIV for HSC convective flow diagnostics, Measurement Science and Technology 15 (2004) 664–672.
[9] W. Hauf, U. Grigull, Optical methods in heat transfer, in: J.P. Harnett, T.F. Irvine Jr. (Eds.), Advances in Heat Transfer, vol. 6, Academic Press, New York, 1970, pp. 133–311.
[10] M. Raffel, C. Willert, J. Konipenhans, Particle Image Velocimetry, Springer-Verlag, Heidelberg, 1998.
[11] Dynamic Studio Manual, Dantec Dynamics A/S, 2006, Publication number: 9040U1081.
[12] Fluent User's Guide, Release 6.2.16, Fluent Incorporated, 2005.